

# Numerical Simulation of Superhalo Electrons Generated by Magnetic Reconnection in the Solar Wind Source Region

L.-P. Yang<sup>1,2</sup>, L.-H. Wang<sup>1</sup>, J.-S. He<sup>1</sup>, C.-Y. Tu<sup>1</sup>, S.-H. Zhang<sup>3</sup>, L. Zhang<sup>1</sup> and X.-S. Feng<sup>2</sup>

<sup>1</sup> School of Earth and Space Sciences, Peking University, 100871 Beijing, China;  
*wanglhwan@gmail.com*

<sup>2</sup> SIGMA Weather Group, State Key Laboratory for Space Weather, Center for Space Science and  
Applied Research, Chinese Academy of Sciences, 100190 Beijing, China

<sup>3</sup> Institute of Geology and Geophysics, Chinese Academy of Sciences, 100029 Beijing, China

**Abstract** Superhalo electrons appear to be continuously present in the interplanetary medium, even at very quiet times, with a power-law spectrum at energies above  $\sim 2$  keV. Here we numerically investigate the generation of superhalo electrons by magnetic reconnection in the solar wind source region, using the MHD and test particle simulations for both single X-line reconnection and multiple X-line reconnection. We find that the direct current electric field, produced in the magnetic reconnection region, can accelerate electrons from an initial thermal energy of  $T \sim 10^5$  K up to hundreds of keV. After acceleration, some of the accelerated electrons, together with the nascent solar wind flow driven by the reconnection, propagate upwards along the newly-opened magnetic field lines into the interplanetary space, while the rest move downwards into the lower atmosphere. Similar to the observed superhalo electrons at 1 AU, the flux of the upward-traveling accelerated electrons versus energy displays a power-law distribution at  $\sim 2 - 100$  keV,  $f(E) \sim E^{-\delta}$ , with a  $\delta$  of  $\sim 1.5 - 2.4$ . For single (multiple) X-line reconnection, the spectrum becomes harder (softer) as the anomalous resistivity parameter  $\alpha$  (uniform resistivity  $\eta$ ) increases. These modeling results suggest that the acceleration in the solar wind source region may contribute to superhalo electrons.

**Key words:** acceleration of particles — methods: numerical — Sun: particle emission — (Sun:) solar wind — Sun: transition region

## 1 INTRODUCTION

Electron measurements from the 3D Plasma and Energetic Particle instrument on the WIND spacecraft near 1 AU find a superthermal component of solar wind electron population at energies above  $\sim 2$  keV, denoted the “superhalo”, with a power-law ( $f(E) \sim E^{-\delta}$  with  $\delta \sim 2.5$ ) spectrum extending to  $> 100$  keV, and a

nearly isotropic angular distribution (Lin 1997, 1998). Superhalo electrons appear to be the electron counterpart of the power-law-tail suprathermal ions above solar wind and pickup ion energies that are observed throughout the heliosphere at all the times (e.g., Gloeckler et al. 2008; Wimmer-Schweingruber et al. 2013). Using high sensitivity measurements from the SupraThermal Electron instrument (Lin et al. 2008) on the STEREO, Wang et al. (2012) reported that the power-law spectral index  $\delta$  of superhalo electrons observed during quiet-times near solar minimum ranges from  $\sim 1.5$  to  $\sim 3.4$ , with an average of  $\sim 2.35 \pm 0.45$ . The observed density of superhalo electrons, about  $10^{-9} - 10^{-6}$  of the solar wind proton density, decreases with the decay of solar cycle, while  $\delta$  has no solar-cycle variation. Since these superhalo electrons are present even in the absence of any solar activity (e.g., active regions, flares, etc.), Wang et al. (2012) suggested that superhalo electrons may be generated by wave-particle interactions in the interplanetary medium (IPM), or by nonthermal processes related to the acceleration of the solar wind.

With a weak turbulence approach, Yoon et al. (2012) proposed that superhalo electrons are accelerated by local resonant interactions with electron beam-excited Langmuir waves and that the dynamic equilibrium between these electrons and Langmuir waves predicts a power-law spectrum of  $E^{-2.3}$ , consistent with observations. However, Podesta (2008) argued that the observed energy density of the Langmuir waves at 1 AU is too small to accelerate superhalo electrons by the time the solar wind reaches 1 AU.

If superhalo electrons arise from the Sun, one possible accelerator is the magnetic reconnection in the solar wind source region. Many researches have examined the charged-particle acceleration by magnetic reconnection in solar flares or the Earth's magnetosphere (e.g., Speiser 1965; Bulanov & Sasorov 1976; Bulanov 1980; Martens & Young 1990; Litvinenko & Somov 1993; Miller et al. 1997; Mori et al. 1998; Browning & Vekstein 2001; Hamilton et al. 2003; Zharkova & Gordovskyy 2004; Wood & Neukirch 2005; Turkmani et al. 2006; Cargill et al. 2006; Onofri et al. 2006; Liu et al. 2009; Drake et al. 2010; Gordovskyy et al. 2010; Oka et al. 2010; Kowal et al. 2011; Li & Lin 2012; Bian & Kontar 2013; Leonardis et al. 2013). Speiser (1965) was the first to analyze the direct current (DC) electric field acceleration in the single reconnecting current sheet (RCS), by analytically solving the particle motion equations in the geomagnetic tail. Based on simulations with the single RCS in solar flare, Mori et al. (1998) obtained a power-law energy spectrum with the index of 2.0-2.2 for the accelerated protons, consistent with the theoretical prediction by Bulanov (1980); Wood & Neukirch (2005) got a power-law energy spectrum with the index  $\sim 1.5$  for the accelerated electrons in the reconnection outflow region. Moreover, Turkmani et al. (2006) and Cargill et al. (2006) found a power-law distribution for the accelerated ions and electrons, from simulations with the stochastic development of transient RCSs. Onofri et al. (2006) also suggested that the fragmented RCSs can be very efficient electron accelerator. Based on two-dimensional particle-in-cell (PIC) simulations of multi-island reconnection, Drake et al. (2010) and Oka et al. (2010) proposed that electron and ion acceleration is dominated by Fermi reflection in contracting and merging magnetic islands. However, the above models related to solar flares may not conform well to the superhalo electrons that are not correlated with flares. Due to their continuous presence in the PM, similar to the solar wind, these superhalo electrons could be produced by the magnetic reconnection related to the solar wind origin (Wang et al.

If the superhalo electrons observed at 1 AU originate from the solar wind source region, then a self-consistent acceleration model would also include the particle-escape process from the Sun to the IPM. One possibility is to involve open magnetic field lines out into the IPM, as suggested by many models of solar energetic particles from the acceleration in transient events such as solar flares and coronal mass ejections (Vainio et al. 2000; Dmitruk et al. 2003; Arzner & Vlahos 2006; Rosdahl & Galsgaard 2010; Baumann & Nordlund 2012; Masson et al. 2012). Recently, we have simulated the reconnection between a closed loop and an open funnel in the solar wind source region, to examine the origin of the solar wind (Yang et al. 2013). In the present study, we utilize this magnetic reconnection model (Section 2.1) and a test particle model (Section 2.2), and simulate the flux energy spectrum and production rate of accelerated electrons by the reconnection electric field in the solar wind source region (Section 3), to investigate the solar origin of superhalo electrons.

## 2 NUMERICAL METHOD

### 2.1 Numerical MHD Model

The numerical MHD model used here has been described in details in Yang et al. (2013). This section only gives the basic features and specifies parameters/initial conditions for this study. In order to sustain conservation laws and correct relationships of quantities across discontinuities in simulations, the 2.5-D resistive MHD equations, in the Cartesian coordinates  $(x, y, z)$  with  $y$  directed vertically, are written in a conservational form. By adopting reference values of the plasma density  $\rho_0 (= 2 \times 10^{-10} \text{ kg m}^{-3})$ , length  $L_0 (= 1 \text{ Mm})$ , and temperature  $T_0 (= 10^4 \text{ K})$ , these equations are normalized as follows:

$$\frac{\partial \rho}{\partial t} + \nabla \cdot \rho \mathbf{u} = 0 \quad (1)$$

$$\frac{\partial \rho \mathbf{u}}{\partial t} + \nabla \cdot \left[ \rho \mathbf{u} \mathbf{u} + \mathbf{I} \left( p + \frac{1}{2} \mathbf{B}^2 \right) - \mathbf{B} \mathbf{B} \right] = \rho \mathbf{g} \quad (2)$$

$$\frac{\partial e}{\partial t} + \nabla \cdot \left[ \mathbf{u} \left( e + p + \frac{1}{2} \mathbf{B}^2 \right) - (\mathbf{u} \cdot \mathbf{B}) \mathbf{B} \right] = \rho \mathbf{u} \cdot \mathbf{g} + \nabla \cdot (\mathbf{B} \times \eta \mathbf{j}) - L_r + \nabla \cdot \mathbf{q} + H + C_N \quad (3)$$

$$\frac{\partial \mathbf{B}}{\partial t} + \nabla \cdot (\mathbf{u} \mathbf{B} - \mathbf{B} \mathbf{u}) = \eta \nabla^2 \mathbf{B} \quad (4)$$

where

$$e = \frac{1}{2} \rho \mathbf{u}^2 + \frac{p}{\gamma - 1} + \frac{1}{2} \mathbf{B}^2, \quad \mathbf{J} = \nabla \times \mathbf{B} \quad (5)$$

correspond to the total energy density and current density, respectively. Here,  $\rho$  is the mass density;  $\mathbf{u} = (v_x, v_y, v_z)$  is the plasma velocity;  $p$  is the thermal pressure;  $\mathbf{B}$  denotes the magnetic field;  $\mathbf{g} (= -g \mathbf{e}_y, g = \text{const})$  is the solar gravitational acceleration;  $\gamma (= 5/3)$  is the adiabatic index;  $L_r$  represents radiative losses;  $\nabla \cdot \mathbf{q}$  gives the anisotropic thermal conduction;  $C_N$  is the Newton cooling term;  $H$  is the parameterized heating term; and  $\eta$  is the magnetic resistivity. Here, we assume two resistivity models of the magnetic reconnection: anomalous resistivity to trigger single X-line reconnection, and uniform resistivity to trigger multiple X-line reconnection.

At the Sun, once the current density  $J$  is larger than the threshold of current-driven micro-instability (such as ion acoustic instability), large enough local diffusion can be triggered to increase the local

Büchner & Elkina 2005). Many theoretical analysis and simulations have reported that the anomalous resistivity strongly depends on  $J$  (Sagdeev 1967; Davidson & Gladd 1975; Petkaki & Freeman 2008; Wu et al. 2010; Bai & Diamond 2010), e.g., in a linear or power-law form. Based on the MHD simulations by Sato & Hayashi (1979), Ugai (1992) and Otto (2001), here we set  $\eta$  in the anomalous resistivity model to be a function of the current density:

$$\eta = \begin{cases} 0, & J \leq J_c \\ \eta_0(J - J_c)^\alpha, & J > J_c \end{cases} \quad (6)$$

where  $\eta_0$  and  $\alpha$  are the resistivity parameters, and  $J_c$  is the current-density threshold above which the anomalous resistivity is triggered. As suggested by Treumann (2001) and Büchner & Elkina (2005),  $\eta_0$  and  $J_c$  are set to be  $0.001 L_0 V_0$  and  $0.5 B_0 L_0^{-1} \mu^{-1}$ , respectively, where  $V_0 (= \sqrt{RT_0})$ ,  $R$  is gas constant) is the reference velocity, and  $B_0 (= \sqrt{\mu \rho_0} V_0$ ,  $\mu$  is magnetic permeability) is the reference magnetic strength. For  $\alpha$ , we simulate for four different values, 0.5, 1.0 (Ugai 1992), 2.0 (Otto 2001), and 3.0 (Sato & Hayashi 1979).

At the Sun, on the other hand, the collisional resistivity is generally too small ( $\ll 10^{-6} \Omega \text{ m}$ ) to be resolved under current computation ability, and to make dissipation difficult (Cargill et al. 2012). In the uniform resistivity reconnection model, thus we simulate with an enhanced  $\eta$ , for three values of  $8 \times 10^{-4}$ ,  $2 \times 10^{-4}$  and  $5 \times 10^{-5}$  (Biskamp & Welter 1980; Samtaney et al. 2009; Onofri et al. 2004, 2006). For a smaller uniform  $\eta$  (e.g.,  $10^{-5}$ ), however, the upward-traveling electrons can not be accelerated to energies above 50 keV in our reconnection model.

In both resistivity models, the simulation region spans  $-13 \text{ Mm} \leq x \leq 0 \text{ Mm}$  in the horizontal dimension and  $0 \text{ Mm} \leq y \leq 15 \text{ Mm}$  in the vertical dimension. This region is covered by a nonuniform grid in both dimensions, with a grid spacing of  $\delta x = \delta y = 25 \text{ km}$  for  $0 \text{ Mm} \leq y < 4 \text{ Mm}$ ,  $\delta x = \delta y = 50 \text{ km}$  for  $4 \text{ Mm} \leq y < 6 \text{ Mm}$ , and  $\delta x = \delta y = 100 \text{ km}$  for  $y \geq 6 \text{ Mm}$ . We use the same boundary conditions defined by Yang et al. (2013).

For the initial conditions, we assume the plasma in hydrostatic equilibrium with the temperature of a hyperbolic tangent function, and derive the plasma pressure and density from the static equation and ideal gas equation (Yokoyama & Shibata 1996). The initial plasma velocity is set to be 0. The initial magnetic field is set to be an open funnel potential field given by Hackenberg et al. (2000), plus a closed loop potential field generated by two infinite straight-line currents in the  $z$ -direction at  $(x = -10 \text{ Mm}, y = -0.7 \text{ Mm})$  and  $(x = 10 \text{ Mm}, y = -0.7 \text{ Mm})$ . We also assume the presence of a relatively weak magnetic field component ( $B_{z0}$ ) in the  $z$ -direction, to allow the guiding center approximation for the particle orbits in the reconnection region, and the effective particle acceleration (Mori et al. 1998; Browning & Vekstein 2001; Wood & Neukirch 2005; Li & Lin 2012).

## 2.2 Test Particle Approach

Provided that the electron gyro-radius (gyro-period) is much smaller than the model scale length (characteristic time), the guiding center approximation is employed in the present simulation. The relativistic

$$\frac{d\mathbf{r}}{dt} = \mathbf{u}_\perp + \frac{(\Upsilon v_\parallel)}{\Upsilon} \mathbf{b} \quad (7)$$

$$\begin{aligned} \mathbf{u}_\perp = \mathbf{u}_E + \frac{m}{q} \frac{(\Upsilon v_\parallel)^2}{\Upsilon \kappa^2 B} [\mathbf{b} \times (\mathbf{b} \cdot \nabla) \mathbf{b}] + \frac{m}{q} \frac{\mu_B}{\Upsilon \kappa^2 B} [\mathbf{b} \times (\nabla(\kappa B))] + \frac{m}{q} \frac{(\Upsilon v_\parallel)}{\kappa^2 B} [\mathbf{b} \times (\mathbf{b} \cdot \nabla) \mathbf{u}_E] \\ + \frac{m}{q} \frac{(\Upsilon v_\parallel)}{\kappa^2 B} [\mathbf{b} \times (\mathbf{u}_E \cdot \nabla) \mathbf{b}] + \frac{m}{q} \frac{\Upsilon}{\kappa^2 B} [\mathbf{b} \times (\mathbf{u}_E \cdot \nabla) \mathbf{u}_E] \end{aligned} \quad (8)$$

$$\frac{d(\Upsilon v_\parallel)}{dt} = \frac{q}{m} \mathbf{E} \cdot \mathbf{b} - \frac{\mu_B}{\Upsilon} (\mathbf{b} \cdot \nabla(\kappa B)) + (\Upsilon v_\parallel) \mathbf{u}_E \cdot ((\mathbf{b} \cdot \nabla) \mathbf{b}) + \Upsilon \mathbf{u}_E \cdot ((\mathbf{u}_E \cdot \nabla) \mathbf{b}) \quad (9)$$

$$\Upsilon = \sqrt{\frac{c^2 + (\Upsilon v_\parallel)^2 + 2\mu_B B}{c^2 - u^2}} \quad (10)$$

In the above equations,  $\mathbf{r}$  is the electron position vector and  $\mathbf{b}(= \mathbf{B}/B)$  is the unit vector of magnetic field  $\mathbf{B}$ ;  $m$  and  $q$  are the electron mass and charge;  $c$  is the speed of light;  $\mathbf{u}_\perp$  is the electron velocity component perpendicular to  $\mathbf{B}$ , including  $\mathbf{E} \times \mathbf{B}$  drifts, curvature drifts and gradient drifts;  $v_\parallel$  is the electron velocity component parallel to  $\mathbf{B}$ ;  $\mu_B$  is the particle magnetic moment.  $\Upsilon(= 1/\sqrt{1 - v^2/c^2})$  is the relativistic factor, where  $v$  is the electron speed, and the coefficient  $\kappa$  equals to  $\sqrt{1 - u_E^2/c^2}$ , where  $\mathbf{u}_E = \mathbf{E} \times \mathbf{b}$ .

Since the acceleration time ( $\sim 0.001$  s) of electrons is much shorter than the characteristic timescale ( $\sim 20$  s) of the RCS evolution in the solar wind source region, we simulate the trajectory and velocity of electrons with quasi-static background field snapshots from our MHD model. We spatially bi-linearly interpolate these MHD model results to obtain  $\mathbf{u}(\mathbf{r})$ ,  $\mathbf{B}(\mathbf{r})$  and  $\mathbf{j}(\mathbf{r})$ , and then calculate  $\mathbf{E}(\mathbf{r})$  via  $\mathbf{E} = -\mathbf{u} \times \mathbf{B} + \eta \mathbf{j}$ . The fourth-order Runge-Kutta method is employed to numerically integrate the motion equations (7)-(9), where the time step ( $\delta t$ ) is adaptive (Zhang et al. 2014). We also assume that electrons are initially distributed uniformly in the transition region, with a Maxwellian velocity distribution of  $T \sim 10^5$  K and no bulk velocity. The rectangle in Figures 1 and 6 denotes the injection region for test electrons. In each case of  $\alpha = 0.5, 1.0, 2.0, 3.0$  and  $\eta = 8 \times 10^{-4}, 2 \times 10^{-4}, 5 \times 10^{-5}$ , about  $10^6$  electron orbits are calculated.

### 3 SIMULATION RESULTS

#### 3.1 Single X-line Reconnection

For single X-line reconnection driven by anomalous resistivity, the overall evolution of the MHD simulation is similar to that in our previous work (Yang et al. 2013). This MHD simulation is not sensitive to the values of  $\alpha$ , consistent with previous studies (Sato & Hayashi 1979; Otto 2001), while  $\alpha$  influences the spectral shape of the accelerated electrons in the test-particle simulation. In this session, we illustrate the detailed simulation results for  $\alpha = 1.0$ , followed by brief descriptions for the other three  $\alpha$  values.

Figure 1 presents a MHD snapshot for  $\alpha = 1.0$ , with the spatial distribution of the temperature  $T$  (a), vertical velocity  $V_y$  (b), out-of-plane current density  $J_z$  (c) and total diffusive electric field  $E_{resi}$  (d), at  $t = 25$  minutes (the early stage of reconnection). We note that carried by the horizontal flow implemented

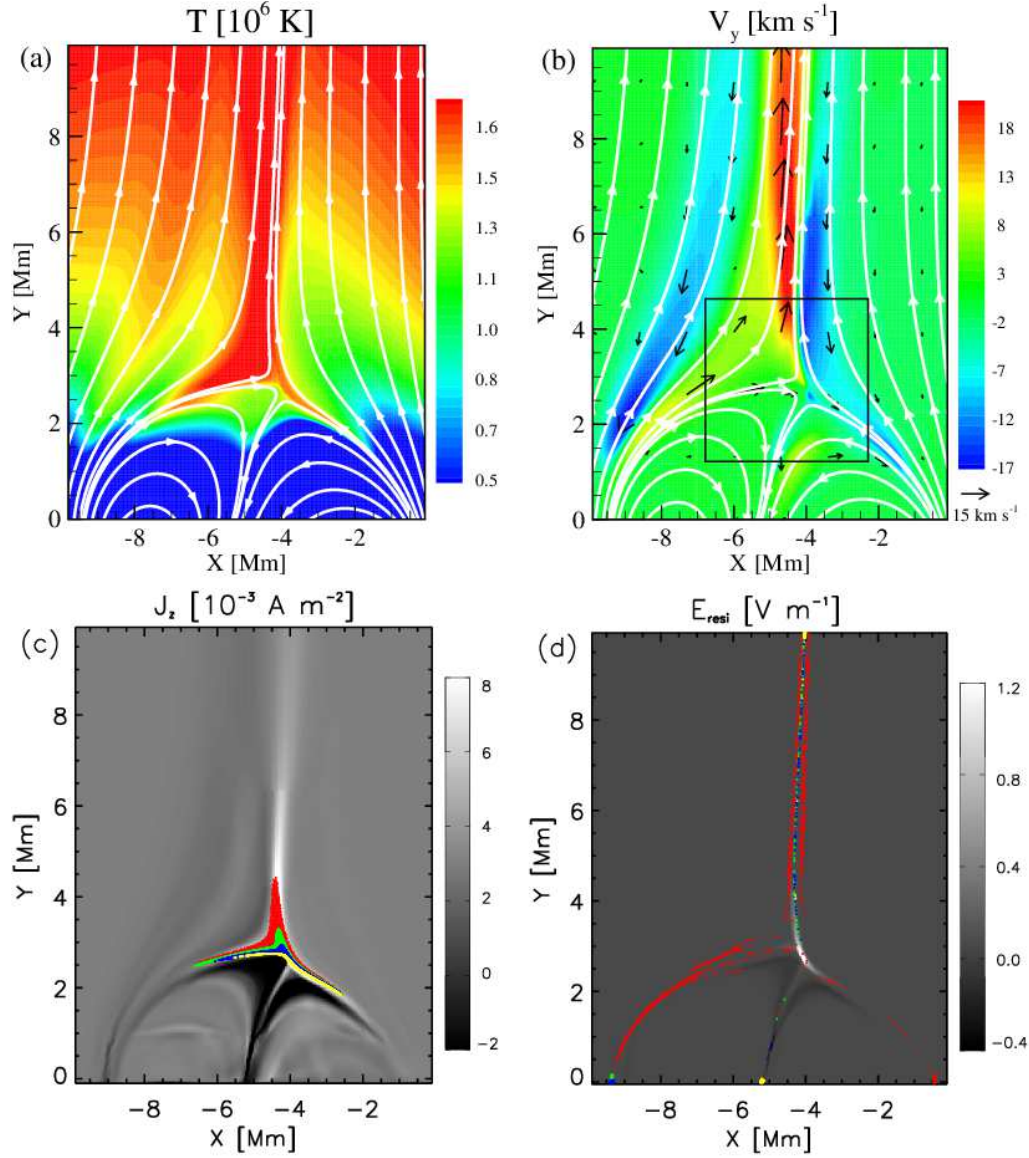


**Fig. 1** Spatial distributions of the plasma temperature  $T$  (a), vertical velocity  $V_y$  (b), out-of-plane current density  $J_z$  (c) and total diffusive electric field  $E_{resi}$  (d) at  $t = 25$  minutes for the anomalous resistivity parameter  $\alpha = 1.0$ . In panel a and b, white streamlines show the magnetic field lines, and black arrows indicate the plasma velocity. In panel c (d), red, green, blue and yellow dots denote the initial (last) positions of electrons over a time interval of 0.1 s, respectively, for the final energy between 2-5 keV, 6-10 keV, 11-60 keV, and 61-200 keV. This MHD snapshot is used for the test particle simulation, with the black rectangle denoting the region where the test electrons are initially injected.

Such reconnection produces both upward and downward outflows in the reconnection region, while the post-reconnection pressure gradient causes a second upward flow along the newly-opened magnetic field lines. In the reconnection region, the large current density  $J$  forms, and the temperature there is enhanced due to Joule dissipation. Once  $J$  exceeds the threshold  $J_c$ , the anomalous resistivity will be switched on. As shown in Figure 1(d), therefore, the diffusive electric field  $E_{resi}(= \eta J)$  builds up in the reconnection



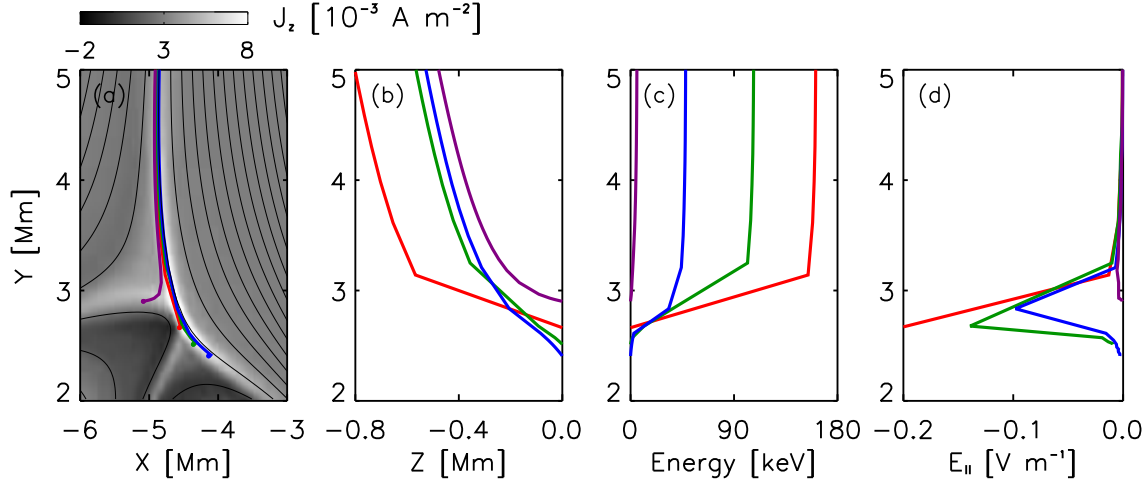


**Fig. 2** (a): the trajectories in the  $x - y$  plane of four sample electrons with the final energy of 6 keV (purple), 48 keV (blue), 107 keV (green) and 161 keV (red), superimposed in the spatial distribution of current density  $J$ , for  $\alpha = 1.0$ . The colored dots indicate the electron initial positions. (b): their trajectories in the  $z - y$  plane. (c-d): the electron energy and  $E_{\parallel}$  versus  $y$ , along the trajectories of these four electrons.

Figure 1(c) and (d) display, respectively, the initial and last positions of electrons over a time interval of 0.1 s, for the final energy between 2-5 keV (red), 6-10 keV (green), 11-60 keV (blue) and 61-200 keV (yellow). In the test particle simulation, initially about  $10^6$  test electrons are distributed uniformly in a rectangular region containing the reconnection site (see Figure 1(b)), with a Maxwellian velocity distribution of  $T \sim 10^5$  K and no bulk velocity. After a time interval of  $\sim 0.1$  s, about  $5 \times 10^4$  electrons (5% of the  $10^6$  test electrons) pass through the reconnection region, where the diffusive electric field component  $E_{\parallel}$  (parallel to  $\mathbf{B}$ ) is large, and all of them are strongly accelerated to energies above 2 keV by  $E_{\parallel}$ . The closer the electrons reach to the region with larger  $E_{\parallel}$ , the higher energy they could gain (see Figure 1(c) and 2). After the acceleration, these accelerated electrons drift out of the reconnection region along the magnetic field lines (see Figure 1(d)). About half of the accelerated electrons move upwards along the newly-opened magnetic field lines into IPM, together with the nascent solar wind flow driven by the reconnection (see Figure 1(d)). On the other hand, the other half of accelerated electrons move downwards into the lower atmosphere, and they would collide with the ambient dense plasma to emit Hard X-rays via non-thermal bremsstrahlung. Such Hard X-ray emissions would be very weak, probably contributing to the quiet-Sun Hard X-rays (e.g., Hannah et al. 2010), since the observed flux of superhalo electrons at 1 AU is only  $\sim 10^5 - 10^6$  of the peak flux of typical solar energetic electron events associated with Hard X-ray bursts.

Figure 2(a) and (b) show the trajectories of four sample electrons with final energy of 6 keV (purple), 48 keV (blue), 107 keV (green) and 161 keV (red). Although the simulation itself is two dimensional in  $x$  and  $y$ , the  $z$ -displacement of electrons is calculated by integrating  $v_z$  over time. Figure 2(c) and (d) show, respectively, the electron energy and parallel electric field  $E_{\parallel}$  along these four trajectories. As electrons move along the magnetic field lines and approach the reconnection region with non-trivial  $E_{\parallel}$ , they start to be energized. The electrons reaching the very center of the reconnection region can be accelerated (by large

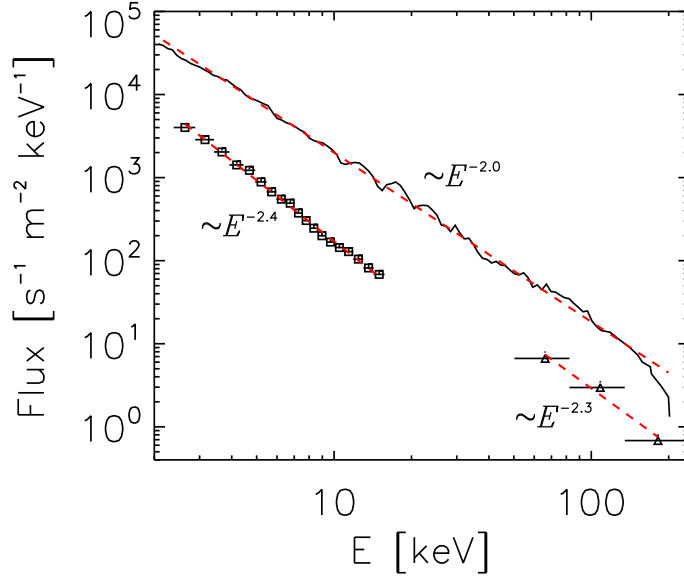


**Fig. 3** Flux versus energy spectrum of upward-traveling electrons with the final energy from  $\sim 2$  keV to 200 keV for  $\alpha = 1.0$ . The squares and asterisks represent the observed superhalo electrons at 1 AU from Wang et al. (2012), with the flux shifted by five orders of magnitude to compare with the simulation results. The red-dash straight lines represent a power-law fit to the simulations results and observations.

the negative  $z$ -direction and reach a maximum displacement up to  $\sim 0.7$  Mm (see Figure 2(b)). Afterwards, electrons leave the reconnection region and move along magnetic field lines mainly in the  $x - y$  plane; the acceleration dramatically decreases.

Figures 1 and 2 suggest that the electric and magnetic field configurations built up by the magnetic reconnection in the solar wind source region are capable of accelerating electrons from thermal to superthermal energies. Assuming a continuous electron injection into the magnetic reconnection region, we calculate the flux of upward-traveling electrons around  $x = -5$  Mm and  $y = 10$  Mm. For  $\alpha = 1.0$  (see Figure 3), the flux versus energy spectrum of electrons at  $\sim 2$ -100 keV fits to a power-law distribution,  $f(E) \sim E^{-2.0}$ . This spectral index  $\delta$  of 2.0 is consistent with the average index ( $2.35 \pm 0.45$ ) of superhalo electrons observed in situ during quiet-time periods (Wang et al. 2012). We also note that in the present simulation, as the magnetic reconnection evolves, the spectral shape of accelerated electrons doesn't change very much.

In the anomalous resistivity model, the energy spectral shape is the most sensitive to the resistivity parameter  $\alpha$ . Here, we also simulate for  $\alpha = 0.5, 2.0$  and  $3.0$ , with the other parameters fixed. Figure 4 compares the spatial distribution of total diffusive electric field  $E_{resi}$  around the reconnection region for  $\alpha = 0.5, 1.0, 2.0$  and  $3.0$ . In the reconnection with asymmetric inflow, the strong diffusive electric field  $E_{resi}$  is built up on the strong field side of RCS. As  $\alpha$  increases, the RCS becomes less flat and  $E_{resi}$  becomes larger, so more electrons can be accelerated to higher energies and the resultant spectrum would become harder (see Figure 5(a)). This is consistent with the simulation by Zharkova & Gordovskyy (2005). In the four  $\alpha$  cases, the flux energy spectra of accelerated electrons above 2 keV all exhibit a single power-



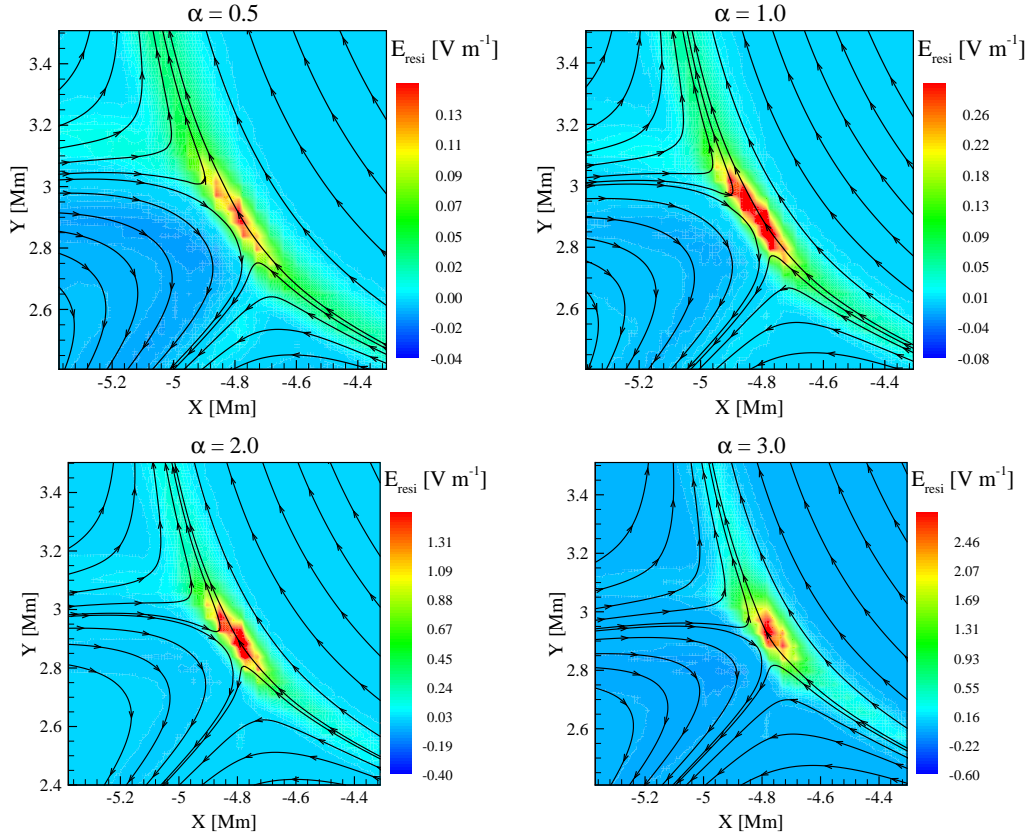


**Fig. 4** A zoomed-in view of spatial distributions of total diffusive electric field  $E_{resi}$  at  $t = 25$  minutes for four simulation cases with  $\alpha=0.5, 1.0, 2.0$  and  $3.0$ , in the area around the reconnection region. Streamlines show the magnetic field lines.

superhalo electrons, while when  $\alpha$  increases to  $3.0$ ,  $\delta$  decreases to  $\sim 1.3$ , harder than the observations (see Figure 5(b)).

### 3.2 Multiple X-line Reconnection

For multiple X-line reconnection driven by small uniform resistivity, we illustrate the detailed simulation results for  $\eta = 2 \times 10^{-4}$ , followed by brief descriptions for  $\eta = 8 \times 10^{-4}$  and  $5 \times 10^{-5}$ . Figure 6 shows the modeled spatial distributions of the plasma vertical velocity  $V_y$  at  $t = 25$  minutes (the early stage of reconnection) for  $\eta = 2 \times 10^{-4}$ . Here the RCS becomes unstable due to tearing instabilities and is fragmented into several magnetic islands. Such magnetic reconnection is no longer the standard Sweet-Parker like, and is inherently time-dependent. In Figure 6, the upward plasma outflow comes not only from the reconnection region, but also from the high-pressure leg of the newly-opened loops, similar to single X-line reconnection. Therefore, this bursty reconnection would not change the mass load to the nascent solar wind outflow as stated by Yang et al. (2013). Since the acceleration time of electrons is much smaller than the characteristic timescale of RCS evolution, we can still use the MHD background field snapshot to conduct test particle simulation, despite the time-dependent reconnection.

In the test particle simulation, initially about  $10^6$  test electrons are distributed uniformly in a rectangular region denoted in Figure 6, with a Maxwellian velocity distribution of  $T \sim 10^5$  K and no bulk velocity. After

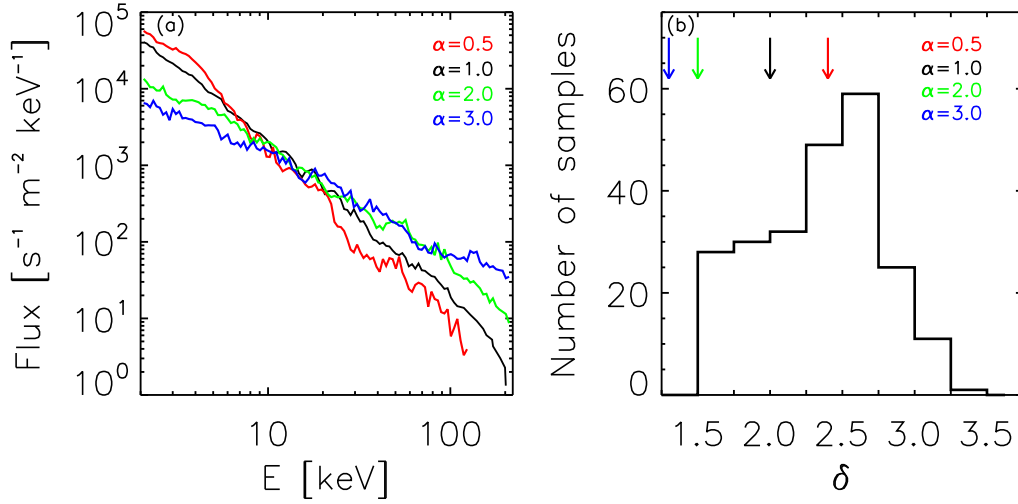


**Fig. 5** a): Comparison of the flux versus energy spectra of accelerated electrons between  $\alpha=0.5$ , 1.0, 2.0 and 3.0, with the other parameters fixed. (b): Histogram of the observed power-law index of superhalo electrons from Wang et al. (2012), with the colored arrows indicating the simulated power-law indexes for the four different  $\alpha$ .

are accelerated to energies above 2 keV by large  $E_{\parallel}$ . After the acceleration, about half of these high-energy electrons move upwards along the newly-opened magnetic field lines into IPM.

Figure 7(a) and (b) show the trajectories of three sample accelerated electrons with the final energy of 6 keV (blue), 30 keV (green) and 110 keV (red), respectively, in the x-y and z-y plane, for  $\eta = 2 \times 10^{-4}$ . Figure 7(c) and (d) display the electron energy and parallel electric field  $E_{\parallel}$ , respectively, along these three trajectories. Compared with single X-line reconnection, the trajectory and energization process of electrons become more complicated in multiple X-line reconnection. For the electrons trapped in magnetic islands (e.g., see the green and red trajectories), they gain high energy as they circle around magnetic islands and experience non-trivial  $E_{\parallel}$ . Note that  $E_{\parallel}$  produced in multiple X-line reconnection is much ( $> 10$  times) weaker than in single X-line reconnection, due to small  $\eta$ . Thus, electrons would travel a longer distance in the  $z$ -direction to acquire a large amount of energy. For the electrons moving freely in open field lines (e.g., see the blue curve), they can undergo multiple accelerations by  $E_{\parallel}$  as they pass by multiple X-lines. However, the final energy gained by these freely moving electrons is limited due to weak  $E_{\parallel}$ .

Figure 8 compares the flux versus energy spectra of accelerated electrons between  $\eta = 8 \times 10^{-4}$ ,  $2 \times 10^{-4}$ , and  $5 \times 10^{-5}$ , with the other parameters fixed. In the three cases, the electron energy spectra above  $\sim 2$  keV generally fit to a single power-law function, with a spectral index  $\delta$  occurring within the range of the observed superhalo electron indexes during quiet-time periods. As  $\eta$  decreases, the RCS becomes thinner and the  $E_{resi}$  away from X-lines gets smaller, so less electrons are produced at energies below  $\sim 20$  keV (although the higher-energy electrons remain essentially unchanged) and the resultant spectrum becomes harder. Our simulations also show that when  $\eta$  decreases below  $\sim 10^{-5}$ , the upward-traveling electrons can not be efficiently accelerated to energies above 50 keV, and thus the simulated energy spectrum is no longer

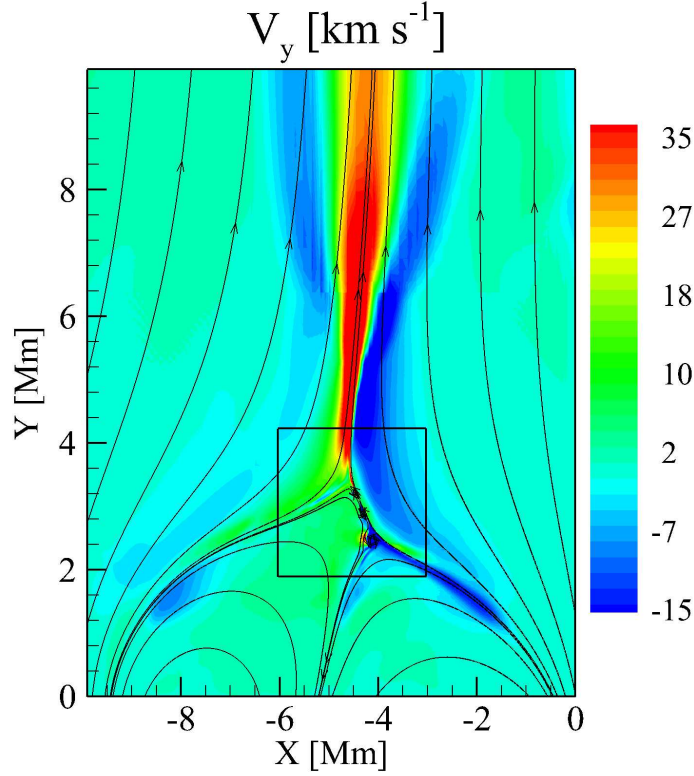


**Fig. 6** Spatial distributions of the plasma vertical velocity  $V_y$  at  $t = 25$  minutes for uniform resistivity  $\eta = 2 \times 10^{-4}$ , with streamlines showing the magnetic field lines. This MHD snapshot is used for the test particle simulation, with the black rectangle denoting the region where test electrons are initially injected.

#### 4 SUMMARY AND DISCUSSION

In this study, we investigate the generation of superhalo electrons under the magnetic reconnection model for the solar wind origin. Using self-consistent electric and magnetic fields obtained from the MHD reconnection simulation, we conduct test particle simulations to study the acceleration of electrons in solar wind source region, for both single X-line reconnection driven by anomalous resistivity and multiple X-line reconnection driven by small uniform resistivity. We find that the superhalo electrons may be contributed by the DC electric field in the magnetic reconnection in the solar wind source region.

The simulation results show that in both reconnection models, electrons with an initial Maxwellian velocity distribution of  $\sim 10^5$  K can be accelerated to high energies, up to hundreds of keV, mainly by the DC electric field in the magnetic reconnection. For single X-line reconnection, electrons gain higher energy as they get closer to the reconnection region, while for multiple X-line reconnection, electrons gain high energy as they are trapped in and circle around magnetic islands. Afterwards, the accelerated electrons follow magnetic field lines to drift out of the reconnection region. About half of the accelerated electrons propagate outwards along the newly-open magnetic field lines into IPM, together with the nascent solar wind flow driven by the reconnection, while the other half move downwards into the lower atmosphere.

In both reconnection models, the energy spectrum of the upward-traveling electrons generally fits well to a single power-law at energies of  $\sim 2 - 100$  keV. For single X-line reconnection, the simulated spectral

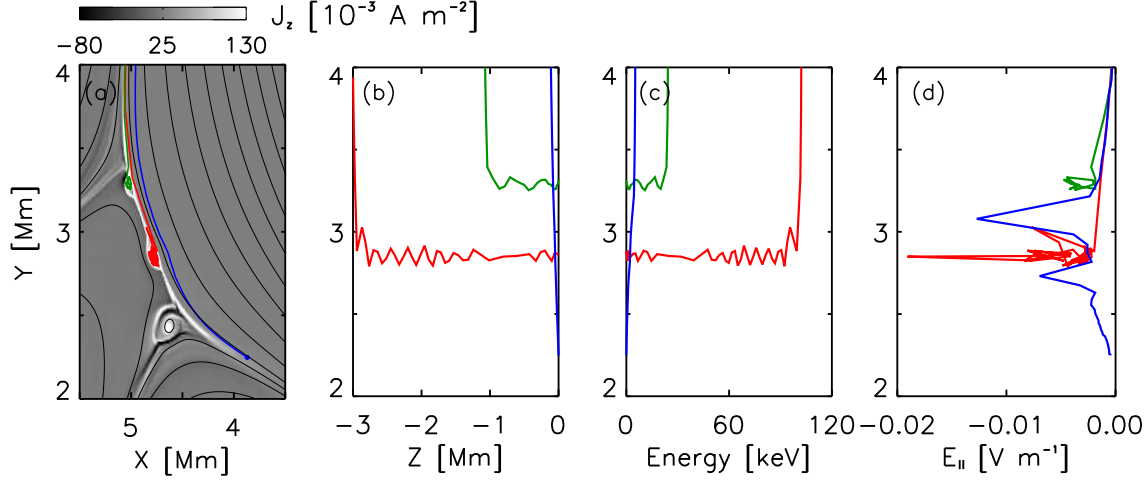


**Fig. 7** (a): the trajectories in the  $x - y$  plane of three sample accelerated electrons with the final energy of 6 keV (blue), 30 keV (green) and 110 keV (red), superimposed in the spatial distribution of current density  $J_z$ , for uniform resistivity  $\eta = 2 \times 10^{-4}$ . The colored dots indicate the electron initial positions. (b): their trajectories in the  $z - y$  plane. (c-d): the electron energy and  $E_{\parallel}$  versus  $y$ , along the trajectories of these three electrons.

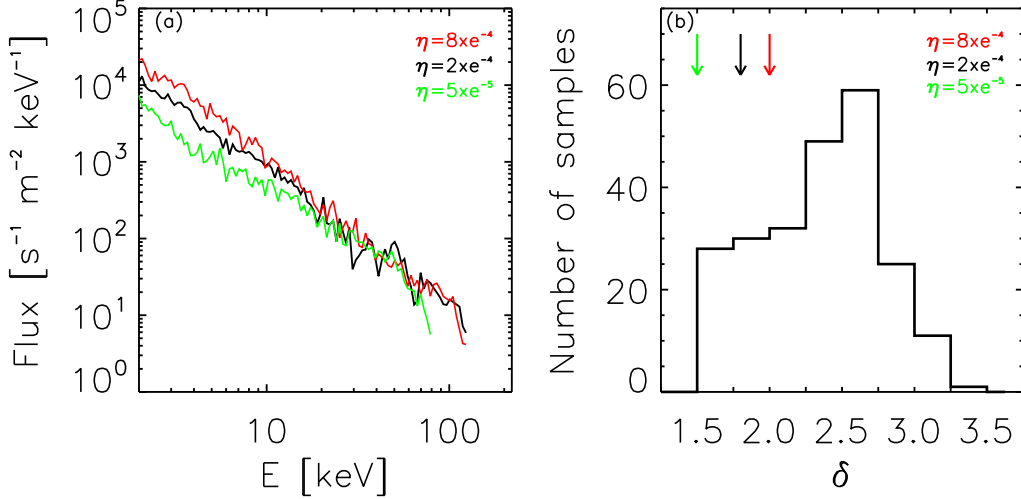


**Fig. 8** Same as Figure 5 but for uniform resistivity  $\eta = 8 \times 10^{-4}$ ,  $2 \times 10^{-4}$ , and  $5 \times 10^{-5}$ .

served during quiet-time periods (Wang et al. 2012). For multiple X-line reconnection, the simulated  $\delta$  is  $\sim 1.5 - 2.0$ , within the index range of superhalo electron observations. Among the model parameters, the resistivity can significantly affect the RCS that, in turn, changes the energy spectrum of accelerated electrons. For single X-line reconnection, as the anomalous resistivity parameter  $\alpha$  increases, more electrons are accelerated to high energies, and thus the simulated spectrum becomes harder. For multiple X-line reconnection, as uniform resistivity  $\eta$  increases, more electrons can be accelerated to energies below 20 keV and the simulated spectrum becomes softer.

Since test particle simulation is not self-consistent, we cannot directly estimate the number density of accelerated electrons and thus their density ratio to the solar wind density in the solar wind source region.

only  $\sim 10\%$  of the electrons passing through the magnetic reconnection region can be accelerated to energies above 2 keV. Using the physical parameters of the MHD simulation as well as this assumption, the density of upward-traveling accelerated electrons above 2 keV is estimated to be  $\sim 10^{-10}$  of the nascent solar wind flow at  $y = 10$  Mm (see Appendix for details). This is close to the in situ superhalo electron observations (Wang et al. 2012), if the number ratio of superhalo electrons to solar wind plasma doesn't vary significantly en route to 1 AU. But note that it is unknown whether the 10% acceleration efficiency assumption is valid in the solar wind source region.

We should note that in the present MHD simulation proposed by Yang et al. (2013), only one closed loop is considered to reconnect with open field lines in the funnel rooted at a chromospheric network conjunction. After the magnetic flux in this closed loop is used up, the reconnection process will cease. To form a continuous and relatively uniform solar wind as observed in the IPM, we need to consider a large number of independent micro reconnection events that happen in a limited time period and in many funnels in the wind source region. Like the reconnection scenario in the solar wind source region (Tu et al. 2005b), this scenario assumes that the successive impulsive reconnection events take place at the interfaces between meso-scale closed loops within the intra-networks and open funnels rooted from the network junctions, to account for the continuous presence of superhalo electro population in the IPM. Those successive impulsive reconnection events may cause local transient events such as bi-directional plasma jets and network brightening (Innes et al. 1997; Chae et al. 2000), as well as large-scale quasi-steady Doppler blue shift in the higher transition region and corona (Tu et al. 2005a; He et al. 2007; Tian et al. 2010). In the future, we will develop a 3-D simulation model to describe the formation of continuous wind from many intermittent micro reconnections and accordingly develop a more realistic particle acceleration model.

This study is mainly aimed at investigating whether the superhalo electrons in the IPM could originate from the Sun. The present model, although simple, is the first to numerically validate this scenario. In future, we can improve this model by considering a comprehensive acceleration, instead of only the DC electric field acceleration. Other mechanisms, such as the turbulence (or stochastic) acceleration, shock acceleration, or collapsing magnetic trap acceleration, could also take place in the reconnection region (Wood & Neukirch 2005). Including these mechanisms would likely allow more electrons to be accelerated to higher energies, increasing the density ratio between the accelerated high-energy electrons and solar wind. Moreover, the Fermi acceleration by reflection from contracting and merging magnetic islands could occur in the multiple X-line reconnection (Drake et al. 2010). As a result of the mismatch between the spatial and temporal scales of the MHD fields and those of electron motion, our MHD models are unable to address this Fermi acceleration; instead, the PIC simulation is usually used to study it (Drake et al. 2010; Oka et al. 2010). At the solar wind source region, however, the very small ion inertial length makes the PIC simulation subject to resolution constraints, reducing the possible physical box size that can be simulated to far below the length scale of the reconnection region. In future, we may also include PIC simulation to examine the influences of the Fermi acceleration by contracting and merging magnetic islands on the results presented here.

Also, we can improve the model by taking into account the effects of Coulomb collisions at the Sun

model would require simulations to be carried out on longer time scales. In simulations with collisions, Gordovskyy et al. (2013) have found that the effect of collisions becomes dominant with time, since the source of acceleration (strong electric field) is transient and thus gradually disappears, while the source of energy losses (coulomb collisions) is always present. Therefore, at the early stage of reconnection, the energy spectra are rather similar to those obtained in simulations with no collisions, while at the later stage when electric fields are gradually decaying, the collisions become dominant. In our test particle simulation for the early stage of reconnection occurring at transition region, we will check the effects of Coulomb collisions on the acceleration of electrons, although such effects may be insignificant. In addition, during the interplanetary propagation, reflection by the interplanetary shocks (e.g., CIR shocks), and/or scattering by wave-particle interaction (e.g., Yoon et al. 2012; Vocks et al. 2005), can isotropize the angular distribution of superhalo electrons, to form a nearly isotropic distribution observed at 1 AU. Also note that the evaluated flux and density of the accelerated electrons in the present model are based upon the value of acceleration efficiency, which can be sensitive to various MHD model parameters, especially to the resistivity parameters. In future, we will consider these respects, to compare the simulations and the observations in details.

**Acknowledgements** This work at Peking University is supported by NSFC under contract Nos. 41274172, 41174148, 40890162, 41222032, and 40931055. L.P. is also supported by NSFC under contract Nos. 41304133, 41031066, 41204127, and 41204105, as well as China Postdoctoral Science Foundation. The numerical calculation has been completed on computing system of Peking University.

## References

- Arzner, K., & Vlahos, L. 2006, *A&A*, 454, 957
- Bai, X. N., & Diamond, P. 2010, in *International Summer Institute for Modeling in Astrophysics*
- Baumann, G., & Nordlund, A. 2012, *The Astrophysical Journal Letters*, 759, L9
- Bian, N. H., & Kontar, E. P. 2013, *Physical Review Letters*, 110, 151101
- Biskamp, D., & Welter, H. 1980, *Physical Review Letters*, 44, 1069
- Browning, P. K., & Vekstein, G. E. 2001, *J. Geophys. Res.*, 106, 18677
- Büchner, J., & Elkina, N. 2005, *Space Sci. Rev.*, 121, 237
- Bulanov, S. V. 1980, *Soviet Astronomy Letters*, 6, 206
- Bulanov, S. V., & Sasorov, P. V. 1976, *Soviet Ast.*, 19, 464
- Cargill, P. J., Vlahos, L., Baumann, G., Drake, J. F., & Nordlund, Å. 2012, *Space Sci. Rev.*, 173, 223
- Cargill, P. J., Vlahos, L., Turkmani, R., Galsgaard, K., & Isliker, H. 2006, *Space Sci. Rev.*, 124, 249
- Chae, J., Wang, H., Goode, P. R., Fludra, A., & Schüle, U. 2000, *ApJ*, 528, L119
- Davidson, R. C., & Gladd, N. T. 1975, *Physics of Fluids*, 18, 1327
- Dmitruk, P., Matthaeus, W. H., Seenu, N., & Brown, M. R. 2003, *The Astrophysical Journal Letters*, 597, L81
- Drake, J. F., Opher, M., Swisdak, M., & Chamoun, J. N. 2010, *ApJ*, 709, 963
- Gloeckler, G., Fisk, L. A., Mason, G. M., & Hill, M. E. 2008, in *American Institute of Physics*



- O. Verkhoglyadova, G. P. Zank, R. P. Lin, & J. Luhmann, 367–374
- Gordovskyy, M., Browning, P. K., Kontar, E. P., & Bian, N. H. 2013, *Sol. Phys.*, 284, 489
- Gordovskyy, M., Browning, P. K., & Vekstein, G. E. 2010, *ApJ*, 720, 1603
- Hackenberg, P., Marsch, E., & Mann, G. 2000, *A&A*, 360, 1139
- Hamilton, B., Mclements, K. G., Fletcher, L., & Thyagaraja, A. 2003, *Sol. Phys.*, 214, 339
- Hannah, I. G., Hudson, H. S., Hurford, G. J., & Lin, R. P. 2010, *The Astrophysical Journal*, 724, 487
- He, J.-S., Tu, C.-Y., & Marsch, E. 2007, *A&A*, 468, 307
- Innes, D. E., Inhester, B., Axford, W. I., & Wilhelm, K. 1997, *Nature*, 386, 811
- Kowal, G., de Gouveia Dal Pino, E. M., & Lazarian, A. 2011, *The Astrophysical Journal*, 735, 102
- Leonardis, E., Chapman, S. C., Daughton, W., Roytershteyn, V., & Karimabadi, H. 2013, *Phys. Rev. Lett.*, 110, 205002
- Li, Y., & Lin, J. 2012, *Sol. Phys.*, 279, 91
- Lin, R. P. 1997, in *Robotic Exploration Close to the Sun: Scientific Basis*, *American Institute of Physics Conference Series*, vol. 385, edited by S. R. Habbal, 25–40
- Lin, R. P. 1998, *Space Sci. Rev.*, 86, 61
- Lin, R. P., Curtis, D. W., Larson, D. E., et al. 2008, *Space Sci. Rev.*, 136, 241
- Litvinenko, Y. E., & Somov, B. V. 1993, *Sol. Phys.*, 146, 127
- Liu, W. J., Chen, P. F., Ding, M. D., & Fang, C. 2009, *ApJ*, 690, 1633
- Martens, P. C. H., & Young, A. 1990, *ApJS*, 73, 333
- Masson, S., Aulanier, G., Pariat, E., & Klein, K.-L. 2012, *Solar Physics*, 276, 199
- Miller, J. A., Cargill, P. J., Emslie, A. G., et al. 1997, *J. Geophys. Res.*, 102, 14631
- Mori, K.-I., Sakai, J.-I., & Zhao, J. 1998, *ApJ*, 494, 430
- Oka, M., Phan, T.-D., Krucker, S., Fujimoto, M., & Shinohara, I. 2010, *The Astrophysical Journal*, 714, 915
- Onofri, M., Isliker, H., & Vlahos, L. 2006, *Physical Review Letters*, 96, 151102
- Onofri, M., Primavera, L., Malara, F., & Veltri, P. 2004, *Physics of Plasmas*, 11, 4837
- Otto, A. 2001, *J. Geophys. Res.*, 106, 3751
- Petkaki, P., & Freeman, M. P. 2008, *The Astrophysical Journal*, 686, 686
- Podesta, J. J. 2008, *Physics of Plasmas*, 15, 122902
- Rosdahl, K. J., & Galsgaard, K. 2010, *A&A*, 511, A73
- Sagdeev, R. Z. 1967, in *Proc. Symposia in Applied Mathematics*, edited by H. Grad, 18
- Samtaney, R., Loureiro, N. F., Uzdensky, D. A., Schekochihin, A. A., & Cowley, S. C. 2009, *Phys. Rev. Lett.*, 103, 105004
- Sato, T., & Hayashi, T. 1979, *Physics of Fluids*, 22, 1189
- Speiser, T. W. 1965, *J. Geophys. Res.*, 70, 4219
- Tian, H., Tu, C., Marsch, E., He, J., & Kamio, S. 2010, *ApJ*, 709, L88
- Treumann, R. A. 2001, *Earth, Planets, and Space*, 53, 453
- Tu, C.-Y., Zhou, C., Marsch, E., et al. 2005a, *Science*, 308, 519
- Tu, C.-Y., Zhou, C., Marsch, E., et al. 2005b, in *Solar Wind 11/SOHO 16, Connecting Sun and Heliosphere*, *ESA Special Publication*, vol. 592, edited by B. Fleck, T. H. Zurbuchen, & H. Lacoste, 131

- Turkmani, R., Cargill, P. J., Galsgaard, K., Vlahos, L., & Isliker, H. 2006, *A&A*, 449, 749
- Ugai, M. 1992, *Physics of Fluids B*, 4, 2953
- Vainio, R., Kocharov, L., & Laitinen, T. 2000, *ApJ*, 528, 1015
- Vocks, C., Salem, C., Lin, R. P., & Mann, G. 2005, *ApJ*, 627, 540
- Wang, L., Lin, R. P., Salem, C., et al. 2012, *ApJ*, 753, L23
- Wimmer-Schweingruber, R. F., Berger, L., & Gloeckler, G. 2013, in *American Institute of Physics Conference Series, American Institute of Physics Conference Series*, vol. 1539, edited by G. P. Zank, J. Borovsky, R. Bruno, J. Cirtain, S. Cranmer, H. Elliott, J. Giacalone, W. Gonzalez, G. Li, E. Marsch, E. Moebius, N. Pogorelov, J. Spann, & O. Verkhoglyadova, 86–89
- Wood, P., & Neukirch, T. 2005, *Sol. Phys.*, 226, 73
- Wu, G., Huang, G., & Ji, H. 2010, *ApJ*, 720, 771
- Yang, L., He, J., Peter, H., et al. 2013, *ApJ*, 770, 6
- Yokoyama, T., & Shibata, K. 1996, *PASJ*, 48, 353
- Yoon, P. H., Ziebell, L. F., Gaelzer, R., Lin, R. P., & Wang, L. 2012, *Space Sci. Rev.*, 173, 459
- Zhang, S., Du, A., Feng, X., et al. 2014, *Solar Physics*, 1–17
- Zharkova, V. V., & Gordovskyy, M. 2004, *ApJ*, 604, 884
- Zharkova, V. V., & Gordovskyy, M. 2005, *Space Sci. Rev.*, 121, 165

## Appendix A: APPENDIX

### A.1. Single X-line reconnection

In the test particle simulation, initially about  $10^6$  test electrons are distributed uniformly in a rectangular region containing the reconnection site (see Figure 1(b)), with a Maxwellian velocity distribution of  $T \sim 10^5$  K. After a time interval of  $\sim 0.1$  s, about  $5 \times 10^4$  electrons (5% of the  $10^6$  test electrons) pass through the reconnection region, where the diffusive electric field component  $E_{\parallel}$  (parallel to  $\mathbf{B}$ ) is large, and all of them are strongly accelerated to energies above 2 keV by  $E_{\parallel}$ . After the acceleration, these accelerated electrons drift out of the reconnection region along the magnetic field lines (see Figure 1(d)), with an average final energy  $K_{ave1} \sim 4$  keV and average final velocity  $V_{ave1} \sim 3.5 \times 10^7$  m s $^{-1}$ . About half of the  $5 \times 10^4$  electrons move upwards along the newly-opened magnetic field lines into IPM, together with the nascent solar wind flow driven by the reconnection (see Figure 1(d)).

Using the physical parameters of the MHD simulation, we can estimate the actual flux, density and total energy gain of the accelerated electrons above 2 keV. In the simulated rectangular region (see Figure 1(b)) with an area  $S_1 = 4.5$  Mm  $\times$  3.5 Mm in the  $x - y$  plane and a depth  $l_1 = 1$  cm in the  $z$ -direction, the actual total number of initial thermal electrons is

$$N_1 = n_0 \times S_1 \times l_1 = 1.6 \times 10^{25}, \quad (\text{A.1})$$

where  $n_0 = 10^8$  cm $^{-3}$  is the background plasma density. According to the test particle simulation, about 5% of the total electrons would pass through the reconnection region and be all accelerated within a time interval of  $\sim 0.1$  s. In a self-consistent simulation, however, not all of them would be accelerated to high

$\sim 10\%$  of the electrons passing through the magnetic reconnection region can be accelerated to energies above 2 keV. In the present simulation, therefore, the physical production rate of the  $> 2$  keV electrons can be estimated as:

$$P_{e1} = (10\% \times 5\% \times N_1)/0.1 \text{ s} = 8 \times 10^{23} \text{ s}^{-1}. \quad (\text{A.2})$$

According to the test-particle simulation, about half of the accelerated  $> 2$  keV electrons would move upwards along the newly-opened magnetic field lines into IPM. At  $y = 10$  Mm, these electrons cross an area  $S_{sup1} \sim 0.2$  Mm (defined as the width at the 1/10-fold peak intensity of electron spatial distribution at the  $x$ -direction)  $\times 1$  Mm (the 1/10-folding width in the  $z$ -direction). Thus, the flux of upward-traveling  $> 2$  keV electrons is  $f_{sup1} = 0.5 \times P_{e1}/S_{sup1}$ , and their number density is

$$n_{sup1} = f_{sup1}/V_{ave1} \sim 5.7 \times 10^4 \text{ m}^{-3}, \quad (\text{A.3})$$

At  $y = 10$  Mm, the average number density of simulated solar wind outflow is  $n_{sw1} \sim 2.7 \times 10^{14} \text{ m}^{-3}$  from the MHD simulation. Then the simulated ratio  $n_{sup1}/n_{sw1}$  is  $2 \times 10^{-10}$  at this altitude.

## A.2. Multiple X-line reconnection

In the test particle simulation, initially about  $10^6$  test electrons are distributed uniformly in a rectangular region denoted in Figure 6, with a Maxwellian distribution of  $T \sim 10^5$  K. After a time interval of  $\sim 0.1$  s, about  $3 \times 10^4$  electrons (3% of the  $10^6$  test electrons) pass through the reconnection region, where the diffusive electric field component  $E_{\parallel}$  (parallel to  $\mathbf{B}$ ) is large, and all of them are strongly accelerated to energies above 2 keV by  $E_{\parallel}$ . After the acceleration, these accelerated electrons drift out of the reconnection region along the magnetic field lines, with an average final energy  $K_{ave2} \sim 3$  keV and average final velocity  $V_{ave2} \sim 3.2 \times 10^7 \text{ m s}^{-1}$ . About half of the  $3 \times 10^4$  electrons move upwards along the newly-opened magnetic field lines into IPM, together with the nascent solar wind flow driven by the reconnection.

Using the physical parameters of the MHD simulation, we can estimate the actual flux, density and total energy gain of the accelerated electrons above 2 keV. In the simulated rectangular region (see Figure 6) with an area  $S_2 = 3 \text{ Mm} \times 2 \text{ Mm}$  in the  $x - y$  plane and a depth  $l_2 = 1 \text{ cm}$  in the  $z$ -direction, the actual total number of initial thermal electrons is

$$N_2 = n_0 \times S_2 \times l_2 = 6 \times 10^{24}, \quad (\text{A.4})$$

where  $n_0 = 10^8 \text{ cm}^{-3}$  is the background plasma density. According to the test particle simulation, about 3% of the total electrons would pass through the reconnection region and be all accelerated within a time interval of  $\sim 0.1$  s. In a self-consistent simulation, however, not all of them would be accelerated to high energies. Then the physical production rate of the  $> 2$  keV electrons can be estimated as:

$$P_{e2} = (10\% \times 3\% \times N_2)/0.1 \text{ s} = 1.8 \times 10^{23} \text{ s}^{-1}, \quad (\text{A.5})$$

for a 10 % acceleration efficiency in the number of electrons passing through the reconnection region (Baumann & Nordlund 2012).

According to the test-particle simulation, about half of the accelerated  $> 2$  keV electrons would move upwards along the newly-opened magnetic field lines into IPM. At  $y = 10$  Mm, these electrons cross an

at the  $x$ -direction, from the test particle simulation)  $\times 0.2$  Mm (the 1/10-folding width in the  $z$ -direction).

Thus, the flux of upward-traveling  $> 2$  keV electrons is  $f_{sup2} = 0.5 \times P_{e2}/S_{sup2}$ , and their number density is

$$n_{sup2} = f_{sup2}/V_{ave2} \approx 3.4 \times 10^4 \text{ m}^{-3}, \quad (\text{A.6})$$

At  $y = 10$  Mm, the average number density of simulated solar wind outflow is  $n_{sw2} \approx 3.4 \times 10^{14} \text{ m}^{-3}$  from the MHD simulation. Then the simulated ratio  $n_{sup2}/n_{sw2}$  is  $10^{-10}$  at this altitude.